

THE PENNSYLVANIA STATE UNIVERSITY
SCHREYER HONORS COLLEGE

DEPARTMENT OF MATERIALS SCIENCE AND ENGINEERING

The Recyclability of Lithium Lanthanum Zirconium Oxide Solid-State
Composite Electrolyte via Cold Sintering

ANTHONY ROMERO
SPRING 2022

A thesis
submitted in partial fulfillment
of the requirements
for a baccalaureate degree in
Materials Science and Engineering
with honors in Materials Science and Engineering

Reviewed and approved* by the following:

Enrique Gomez
Professor of Chemical Engineering and Materials Science and Engineering
Thesis Supervisor

Robert Allen Kimel
Associate Teaching Professor of Materials Science and Engineering
Honors Adviser

* Electronic approvals are on file.

ABSTRACT

With limited resources in a continuously growing global Li-ion battery industry, the recyclability of each component is paramount towards establishing a sustainable future. In this study, one promising recyclable solid-state composite electrolyte, lithium magnesium lanthanum strontium zirconium oxide (LLZO-SM, $\text{Li}_{6.95}\text{Mg}_{0.15}\text{La}_{2.75}\text{Sr}_{0.25}\text{Zr}_2\text{O}_{12}$) paired with polypropylene carbonate (PPC, $(\text{CH}(\text{CH}_3)\text{CH}_2\text{OCO}_2)_n$) and lithium perchlorate (LiClO_4), reprocessed via the cold sintering process (CSP) was investigated. By applying uniaxial pressure and incorporating transient solvents, the CSP allows for the use of lower sintering temperatures, between 25–200°C, and thereby the addition of PPC and LiClO_4 to reduce grain boundary resistance. The work below summarizes a viable processing method to recycle LLZO-SM and a method to further increase ionic conductivity during reprocessing.

TABLE OF CONTENTS

LIST OF FIGURES	iii
LIST OF TABLES	iv
ACKNOWLEDGEMENTS	v
INTRODUCTION	1
Objective	2
BATTERY COMPONENTS AND FUNCTIONALITIES	3
MATERIALS AND METHODS	8
LLZOs Structure and Properties	8
Cold Sintering Process	11
Pristine Half Cell Assembly Methodology	12
Electrochemical Impedance Spectroscopy Methodology	14
Reprocessed Half Cell Assembly Methodology	15
Li-ion Transport Activation Energy	16
X-ray Diffraction of LLZO-SM Powder Methodology	17
RESULTS AND DISCUSSION	18
The Viability of using Cold Sintering	18
Improving Ionic Conductivity	21
Li-ion Transport Activation Energy	24
X-ray Diffraction Analysis	25
CONCLUSIONS	28

LIST OF FIGURES

Figure 1. Labeled active and non-active battery components in a traditional Li-ion battery..	3
Figure 2. Illustrates the charged to fully charged state of a (a) metallic electrode (e.g., lithium metal) and (b) insertion type electrode (e.g., graphene).....	4
Figure 3. Cell architectures and components of (a) a coin cell (b) pouch cell, (c) 18650 cell, and (d) prismatic cell.	7
Figure 4. Garnet crystal structure of (a) c-LLZO and (b) t-LLZO.....	9
Figure 5. (a) c-LLZO's three-dimensional Li-ion migration pathway and loop-like Li atomic site arrangement in (b) c-LLZO and (c) t-LLZO.....	10
Figure 6. The three stages of the cold-sintering process.	12
Figure 7. Cold sintering assembly.....	13
Figure 8. Coin cell assembly.....	14
Figure 9. (a) Simplified EIS circuit model and (b) expected Nyquist plot.	15
Figure 10. Recyclability loop of reprocessing LLZO-SM.	16
Figure 11. Sample 1 LLZO-SM composite (a) pristine vs reprocessed EIS curve and (b) reprocessed ionic conductivity (S/cm) and relative density (%) trend up to the fifth reprocessing.	19
Figure 12. LLZO-SM composite sample 2 composite reprocessed ionic conductivity (S/cm) and relative density (%) trend up to the fourth reprocessing.	20
Figure 13. 150°C preheated LLZO-SM reprocessed ionic conductivity (S/cm) and relative density (%) trend up to the fourth reprocessing.....	22
Figure 14. Comparing non-heated and heated LLZO-SM composite samples relative conductivity (%) and thicknesses (t) per reprocessing cycle.	24
Figure 15. LLZO-SMs reprocessed conductivity as a function of temperature for a (a) heat treated and (b) non-heat-treated reprocessed sample.	25
Figure 16. XRD analysis of LLZO-SM powder exposed to relative humidity (RH), RH and ambient conditions (STP), and RH, STP, and heat-treatment.....	26

LIST OF TABLES

Table 1. c-LLZOs site, occupancy (g), and coordinate parameters.....	8
Table 2. t-LLZOs site, occupancy (g), and coordinate parameters.	8
Table 3. Sample 1 amount of acetonitrile (ACN), di-methylformamide (DMF), weight loss (W_1), thickness (t), mass (m), geometric density of the sample (ρ_o), relative density (RD), real impedance (ReZ), and ionic conductivity (σ_{ion}).	19
Table 4. Sample 2 amount of acetonitrile (ACN), di-methylformamide (DMF), weight loss (W_1), thickness (t), mass (m), geometric density of the sample (ρ_o), relative density (RD), real impedance (ReZ), and ionic conductivity (σ_{ion}).	20
Table 5. Common LLZO reactions when exposed to ambient conditions.	21
Table 6. Pre-heated LZO-SM samples amount of acetonitrile (ACN), di-methylformamide (DMF), weight loss (W_1), thickness (t), mass (m), geometric density of the sample (ρ_o), relative density (RD), real impedance (ReZ), and ionic conductivity (σ_{ion}).....	22

ACKNOWLEDGEMENTS

I would like to thank my thesis supervisor, Dr. Enrique Gomez, for his feedback and time throughout the duration of the project, as well as my honors advisor, Dr. Robert Kimel, for his helpful feedback and suggestions.

I would also like to express my utmost gratitude to my graduate student advisor, Yi-Chen Lan, for taking the time to bring me on board the project, train and assist me in all aspects of the procedures, and the countless times she has supported me in my research endeavors.

In addition, I would like to acknowledge and give my thanks to the technical staff members in the Millennium Science Complex, such as Jeff Long, Dr. Amira Meddeb, and Gino Tambourine, for training me on electrochemical impedance spectroscopy, furnace usage, and X-ray diffraction, respectively.

Additionally, I would like to thank some of the most influential research mentors I have had during my undergraduate pursuit at Penn State, such as Dr. James Goff, Dr. Collin Wilkinson, Rebecca S. Welch, and Dr. James Fleetwood, for giving me their time, sharing their wisdom, and helping me grow into the person I am today.

Lastly, I would like to thank all my family and friends for their endearing support of my work for past four years – culminating into so many lifelong memories I will forever cherish.

INTRODUCTION

Currently, Li-ion batteries (LiBs) dominant the market due to their desirably high volumetric and gravimetric energy density. However, since LiBs commercial debut in the 1990's, lithium metal batteries (LiMBs), having a higher gravimetric and volumetric energy density than LiBs, have been at the forefront of academic and industrial research interest [1]. Unfortunately, when LiMBs are paired with traditional liquid organic electrolytes, LiMBs are thermally and electrochemically unstable [2] and pose catastrophic safety concerns when temperatures exceed 60°C [3]. And with the market value of the current battery industry projected to increase to upwards of \$87.5 billion by 2027 [4], recycling at any stage of a batteries life is becoming increasingly paramount towards establishing a more circular economy.

One promising solution to effectively utilize LiMBs with minimal safety concerns, as well as shows recyclability potential are solid state electrolytes (SSEs). One such ideal SSE is cubic $\text{Li}_7\text{La}_3\text{Zr}_2\text{O}_{12}$ (c-LLZO), because of the materials intrinsically high operating voltage range (0 ~5V) [5,6], excellent thermal stability (25 – 300°C) [7], high mechanical strength to suppress dendrite growth [8], relatively high ionic conductivity ($\sigma > 10^{-4} \text{ Scm}^{-1}$) [9], and low activation energy (0.25-0.28eV) for Li-ion transport [10]. In addition, these properties can be further enhanced through selective doping and/or adding additional materials (i.e., polymers and lithium salts) to create superior composites [10-15].

The LLZO in this study, provided by Spark Plug Co., Ltd, has been doped with magnesium and strontium (hereon referred to as LLZO-SM) to improve the ionic conductivity, reduce grain boundary resistance, and act as a sintering and densification aid [15-17]. Additionally,

polypropylene carbonate and lithium perchlorate salt were added to the composition to create a polymer-salt matrix and serve as a polymer-salt highway for lithium diffusion along grain boundaries. To achieve the desired SSE pellet for battery coin cell testing, the LLZO-SM powder was prepared via cold sintering, a revolutionary sintering process that significantly reduces traditional sintering temperatures by uniaxially applying pressure and heat to incite densification [18].

The preceding chapters in this text will provide a brief overview of a batteries fundamental components, their functions, and considerations, a materials science background on LLZO and cold sintering, discuss the methodology and results of the experiments conducted, and conclude the effectiveness of recycling a LLZO-SM composite utilizing the cold sintering densification process.

Objective

The objective of this thesis is to optimize the processing of a solid-state ceramic-polymer-lithium salt composite electrolyte, lithium magnesium lanthanum strontium zirconium oxide (LLZO-SM, $\text{Li}_{6.95}\text{Mg}_{0.15}\text{La}_{2.75}\text{Sr}_{0.25}\text{Zr}_2\text{O}_{12}$) paired with polypropylene carbonate ($\text{CH}(\text{CH}_3)\text{CH}_2\text{OCO}_2$)_n and lithium perchlorate (LiClO_4) respectively, to achieve a safe, high performance, recyclable solid-state electrolyte. The effectiveness of the synthesis process was measured and characterized through calculating ionic conductivity and x-ray diffraction analysis. The goal of this work is to gain fundamental insights as to how to maintain sufficiently high ionic conductivity as the number of times a sample is recycled/reprocessed increases by modifying physical parameters such as sintering temperature, pressure, and time.

BATTERY COMPONENTS AND FUNCTIONALITIES

A batteries fundamental components can be broken down into two overarching elements, the active and the non-active, shown in Figure 1.

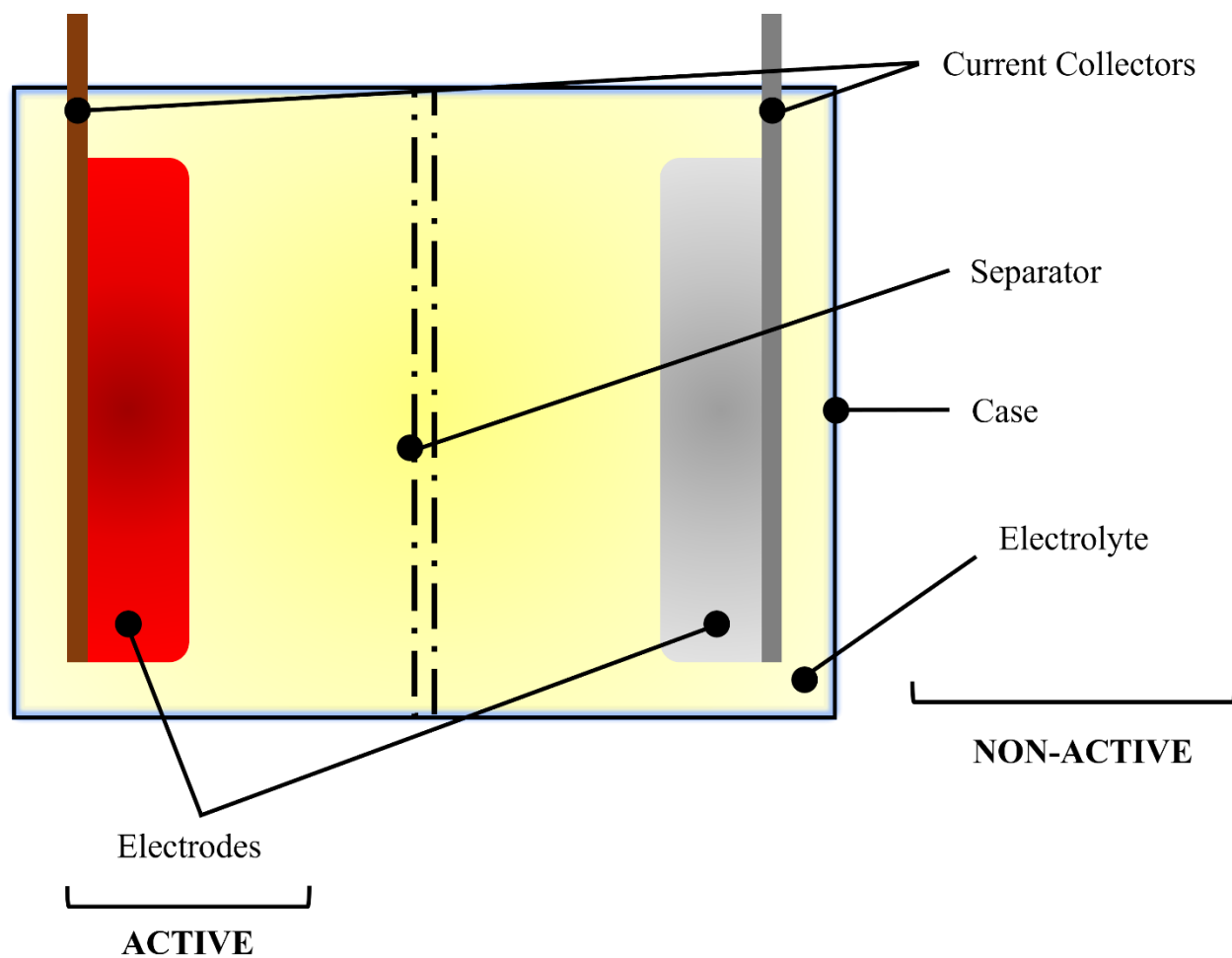


Figure 1. Labeled active and non-active battery components in a traditional Li-ion battery.

The active components consist of two electrodes, referred to as the positive and the negative electrode. At the negative electrode, an oxidation reaction occurs (i.e., electrons are given away as a product). An example of an oxidation reaction using graphite is provided, shown in Equation 1.



The complimentary reaction, a reduction reaction, occurs at the positive electrode (i.e., electrons are accepted). A common positive electrode used in LiBs, lithium iron phosphate, is shown in Equation 2.



There are two classes of electrode materials, metallic (also referred to as “blocking”) electrodes and insertion type (“non-blocking”) electrodes, shown in Figure 2.

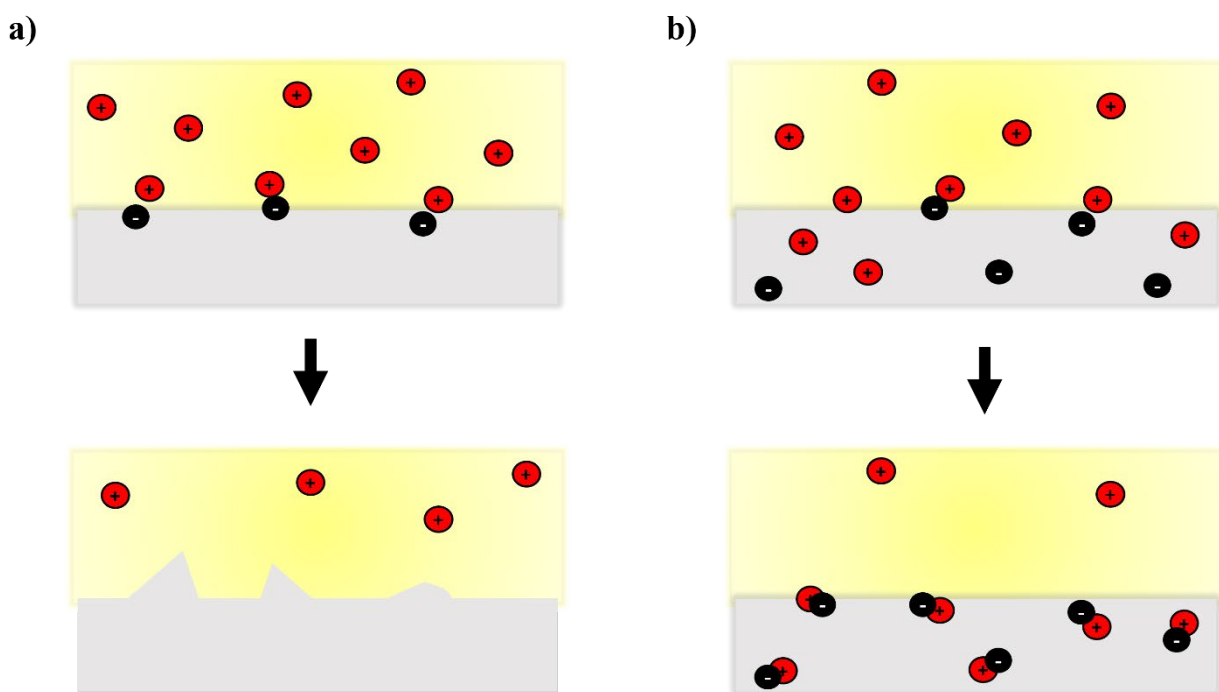


Figure 2. Illustrates the charged to fully charged state of a (a) metallic electrode (e.g., lithium metal) and (b) insertion type electrode (e.g., graphene).

A metallic electrode is defined by having the electrochemical reaction take place at only the surface of the material, such as the lithium metal in LiMBs. An insertion type electrode is defined by undergoing an electrochemical reaction at the surface and bulk of the material. For example, graphene is a common negative insertion type electrode. These fundamental electrode classes are highlighted within this text because all important electrochemical reactions occur at electrode-electrolyte interface, and current research is still striving to gain further insights into this regime to better improve current and future battery chemistries [19].

The non-active components of a battery, illustrated in Figure 1, consist of the electrolyte, separator, current collectors, and casing. A typical liquid electrolyte used in LiBs chemistry solutions are encompassed by one or more dissolved salts and physically contact all components within the cell. The purpose of the electrolyte is to act as an ion conductor between electrodes. The difference between a liquid electrolyte and a solid-state electrolyte is the presence of liquid content. As the name implies, a solid-state electrolyte is entirely solid, which is where the diffusion occurs, and a liquid electrolytes diffusion occurs through a liquid solution. Ensuring the electrolyte is not electrically conductive, electrochemically stable within the applications desired voltage range, non-corrosive to the electrode materials chemistries, has high interfacial contact, and has limited side-reaction during cycling to ensure high coulombic efficiency in early cycle-life testing are all important parameters to keep in mind when selecting/designing your electrochemical cell [19].

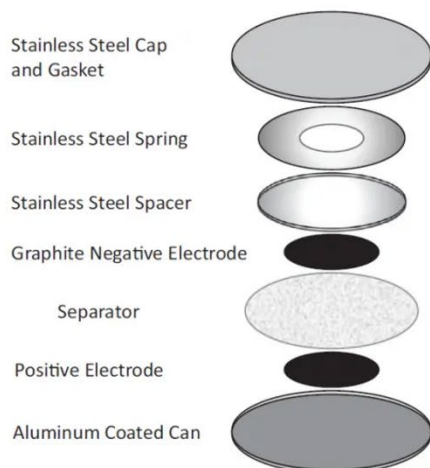
The separator in LiBs is typically a porous polymer placed between the negative and the positive electrode, which acts as a barrier to prevent contact between electrodes (i.e., avoid short circuiting the cell) as well as provides the pathway ions travel through the electrolyte during cycling. How long it takes to sufficiently absorb the electrolyte to minimize internal resistance, the

degree of porosity, the chemical stability, and the mechanical strength are all crucial factors to consider when optimizing a separator [19-21].

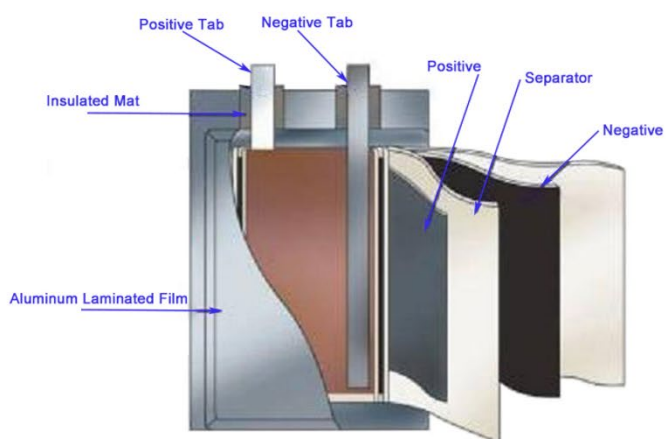
The current collectors are what the electrode is coated onto, with the purpose of transporting electrons during the electrochemical process through an external circuit, charging/discharging the cell. Typical current collectors, such as copper at the negative electrode and aluminum at the positive electrode, need to be light, highly electrically conductive, non-corrosive in the electrolyte solution, mechanically robust, and capable of dispersing heat generated during charging [19].

Finally, the case of a battery varies from cell format to format. A case is typically either plastic(s), typically used in pouch cells, or metal, used in cylindrical, prismatic, and coin cells. The purpose of the casing is to prevent the liquid electrolyte from evaporating from the cell and provide overall mechanical protection and strength to the encompassing components within. Figure 3 illustrates various conventional LiBs cell architectures, such as a coin cell, pouch cell, 18650 cell, and prismatic cell [19, 22-25].

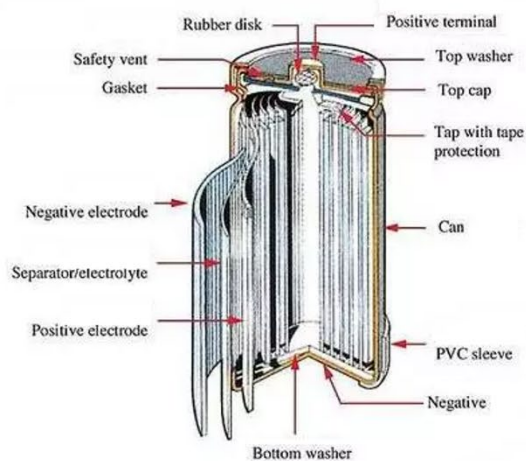
a)



b)



c)



d)

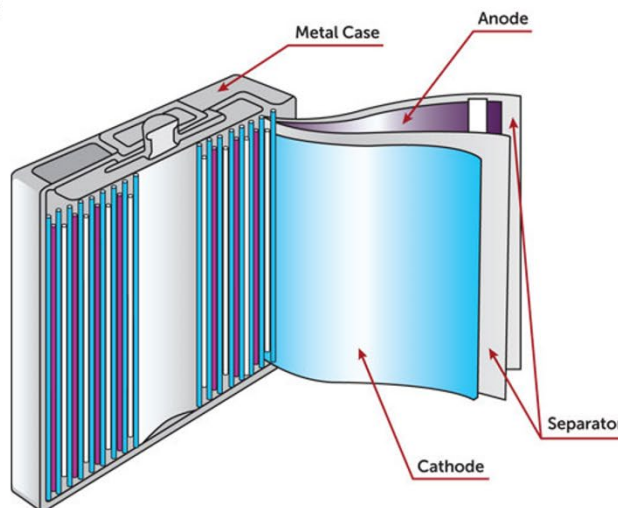


Figure 3. Cell architectures and components of (a) a coin cell (b) pouch cell, (c) 18650 cell, and (d) prismatic cell.

MATERIALS AND METHODS

LLZOs Structure and Properties

Lithium lanthanum zirconium oxide (LLZO) belongs to a class of garnet materials consisting of two polymorphs, cubic (c-LLZO) and tetragonal (t-LLZO), shown in Figure 4 [26,27], with a generic chemical makeup of $\text{Li}_7\text{La}_3\text{Zr}_2\text{O}_{12}$. In c-LLZO, Li occupies tetrahedral 24d and octahedral 96h sites, and La and Zr are eight- and six-fold oxygen coordinated respectively, shown in Figure 4a. Further information about structural parameters have been provided in Table 1 [26]. In t-LLZO, Li occupies tetrahedral 8a, octahedral 16f, and octahedral 96h sites, shown in Figure 4b. Again, further structural information has been provided in Table 2 [27].

Table 1. c-LLZOs site, occupancy (g), and coordinate parameters.

Atom	Site	g	x	y	z
Li ₁	24d	0.94	3/8	0	1/4
Li ₂	96h	0.349	0.0959	0.6922	0.5731
La	24c	1	1/8	0	¼
Zr	16a	1	0	0	0
O	96h	1	-0.0316	0.0538	0.0107

Table 2. t-LLZOs site, occupancy (g), and coordinate parameters.

Atom	Site	g	x	y	z
Li ₁	8a	1	0	1/4	3/8
Li ₂	16f	1	0.0181	0.4313	1/8
Li ₃	32g	1	0.0796	0.0863	0.8099
La ₁	8b	1	0	1/4	1/8
La ₂	16e	1	0.1272	0	1/4
Zr	16e	1	0	0	0
O ₁	32g	1	-0.0355	0.0546	0.1528
O ₂	32g	1	0.0534	0.8525	0.5366
O ₃	32g	1	0.1499	0.0273	0.4454

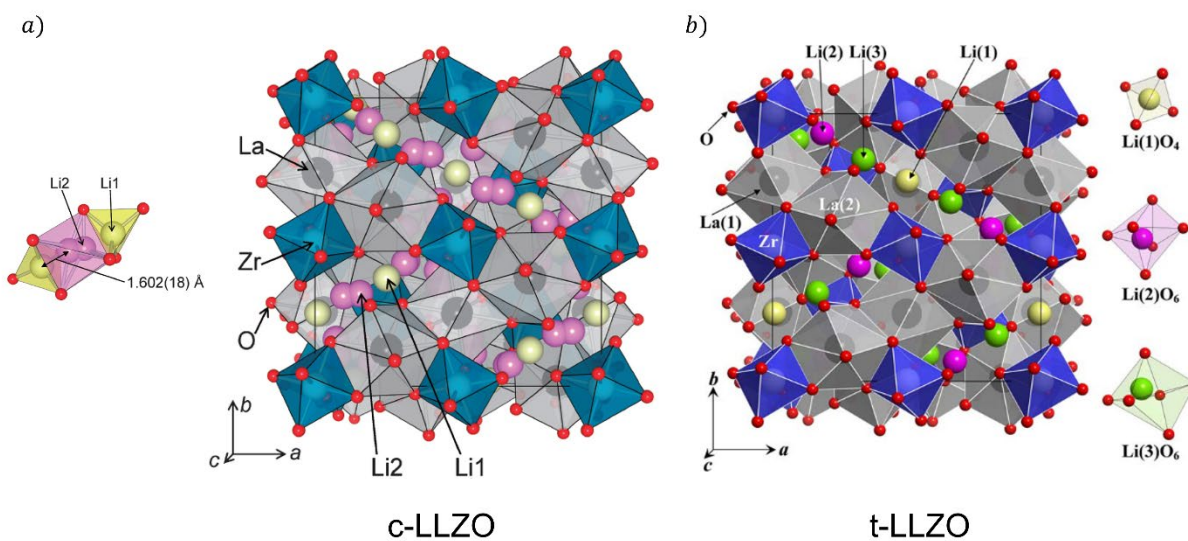


Figure 4. Garnet crystal structure of (a) c-LLZO and (b) t-LLZO.

While very similar in structure, only differing in Li distribution [15], c-LLZO is preferred over t-LLZO because c-LLZOs ionic conductivity can range anywhere from two orders of magnitude higher than t-LLZO [9]. This drastic difference in ionic conductivity is a result of differing Li-ion migration arrangements within each phases structure, shown in Figure 5 [26].

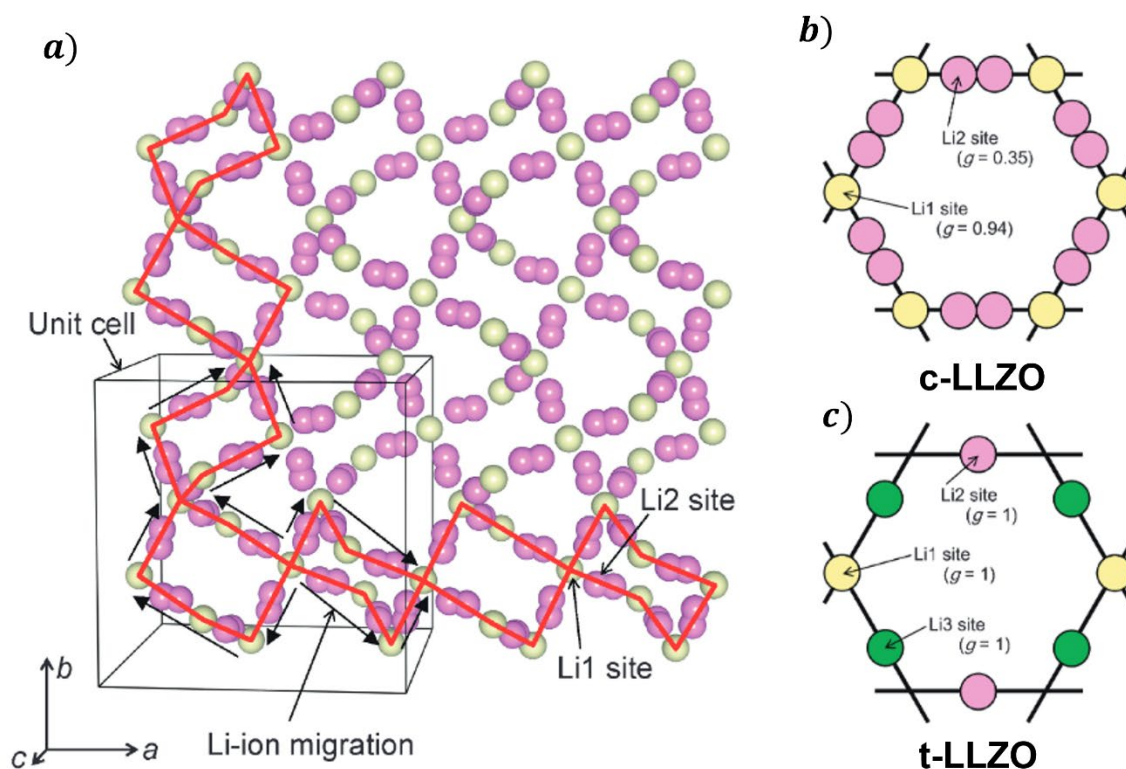


Figure 5. (a) c-LLZOs three-dimensional Li-ion migration pathway and loop-like Li atomic site arrangement in (b) c-LLZO and (c) t-LLZO.

For an 8 per formula unit cell, Li in t-LLZO can occupy a total of 56 occupational sites (8a, 16f, and 32g), stabilizing the structure and leaving no vacancies. While c-LLZO has a total of 120 occupational sites, thereby leaving 64 empty vacancies. This drastic increase in vacancies between the two phases enables higher Li-ion mobility and thus is the reason c-LLZOs structure is more desirable and better optimized for higher Li-ion conductivity for solid-state battery applications [28]. Unfortunately, due to the increased thermodynamic stability from lack of vacancies, t-LLZO is more stable at room temperature than c-LLZO. Thus, additional steps must be taken to stabilize the cubic phase [27].

The most effective ways to stabilize the cubic phase and further enhance ionic conductivity has been proven through doping LLZO. Substituting lithium with elements such as Al^{3+} , Ga^{3+} , Zn^{2+} ,

or Fe^{3+} creates lithium vacancies for higher ionic conductivity. Substituting zirconium with transition/post-transition metals such as Ge^{4+} , Nb^{5+} , Ta^{5+} , Sc^{3+} optimizes the size of ion migration pathways and lithium concentration in the structure [12, 15, 28-31]. Lastly, substituting lanthanum with alkaline earth metals such as Mg^{2+} , Ca^{2+} , and Sr^{2+} has been shown to increase the content of Li at the more mobile Li_1 site and decrease at the Li_2 site, illustrated in Figure 5(b-c) – leading to overall improvement in ion conductivity and reduction in grain boundary resistance [15, 28-32]. In particular, Sr^{2+} is uniquely beneficial to the system at large, as it also acts as a sintering aid [16, 17, 32]. In this work, LLZO has been doped with Sr and Mg (LLZO-SM).

Cold Sintering Process

Outside of doping, the ionic conductivity of LLZO-SM matrix can be further increased through compositing with polymer and lithium salts [14]. Typically, the high sintering temperatures of LLZO $\sim 1100^\circ\text{C}$ [33] would prevent this inclusion, however using the cold sintering process enables simultaneous sintering at relatively low temperatures ($25\text{--}200^\circ\text{C}$) [13, 14, 34].

Three stages have been proposed to occur during the cold sintering process, 1) particle compaction, 2) dissolution-precipitation, 3) and sintering, shown in Figure 6, wherein the densification and mass transport during sintering are enhanced via liquid-enhanced creep, concentration gradients at liquid-liquid interfaces, and concentration gradients at liquid-solid interfaces [34-36].

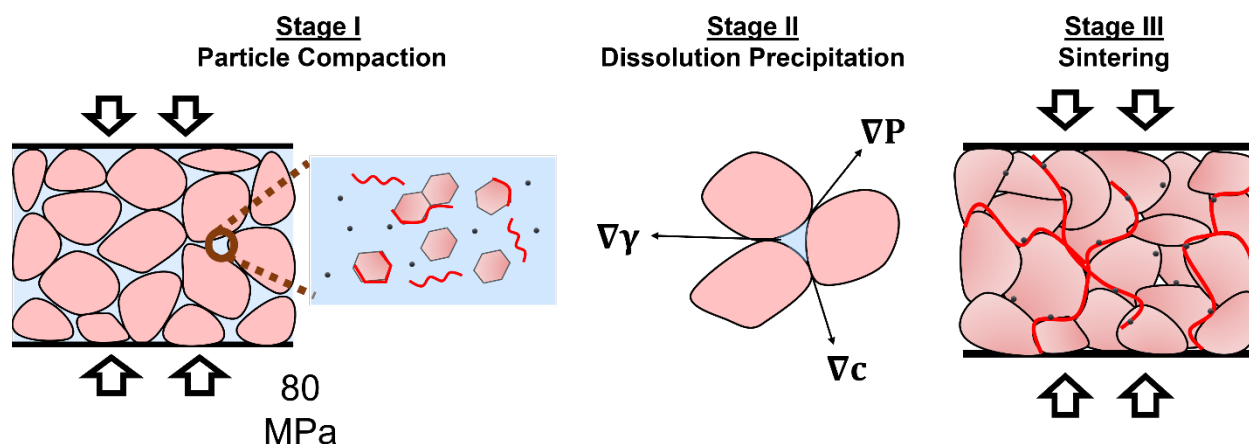


Figure 6. The three stages of the cold-sintering process.

By far the most crucial component of the cold sintering process is selecting a compatible transient solvent that encourages active dissolution of the particles in question. Considering LLZO-SM is known to form Li_2CO_3 at its surface when exposed to the ambient moisture, which exhibits a significantly decreased ionic conductivity and thus considered an impurity, a non-aqueous transient solvent, such as di-methylformamide (DMF), should be selected [14].

Pristine Half Cell Assembly Methodology

A control polymer salt solution consisting of polypropylene carbonate (PPC) and lithium perchlorate (LiClO_4) was prepared by dissolving 13.33 wt% PPC in 80wt% acetonitrile, stirring for several hours. Then the remaining 6.67 wt% LiClO_4 was added to the solution.

Next, in an Ar backfilled glovebox, 480 ± 10 mg of LLZO-SM powder, supplied by NGK Spark Plug Co., Ltd., was grinded into fine powder using a mortar and pestle. Then 120 μL of the control solution and 40 μL of di-methylformamide (DMF) is added to the powder in the mortar. Once again, the powder is grinded down while going through a brief transition of paste to dried

powder again. This dried wetted powder was then added to a 1.27 cm diameter stainless steel die. Inside the die the powder is sandwiched between a piece of aluminum foil, contacting the powder, and mylar, in contact with the stainless steel punch and aluminum foil, easily shown in Figure 7.

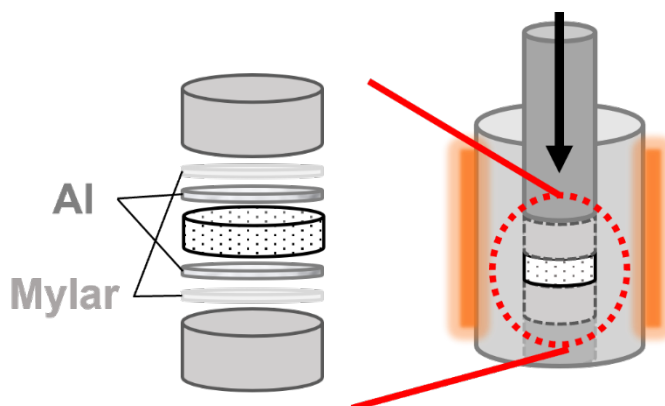


Figure 7. Cold sintering assembly.

The exterior of the die is then surrounded by a heating jacket with a thermocouple in contact with both the jacket and the die. The apparatus is then loaded onto a uniaxial press, followed by applying 80 MPa and 100°C for 1 hour. Afterwards the pressure was slowly released and the cold sintered pellet was carefully removed from the die. The Mylar stuck to the sample was removed using scotch tape, leaving only the Al current collectors. The sample was then weighed, and the thickness measured. The density of the sample was determined geometrically determined using the mass and volume of the pellet, subtracting the accounted thickness and mass of Al foil used. In an idealized state, the pellet would have a mass slightly higher than 0.5000g due to the ~3wt% DMF retained in the composite.

Afterwards, the cell is assembled into a CR2032 coin cell, using a spring, and a combination of 0.5 and 0.2 mm spacers, shown in Figure 8, so that the total thickness of the electrode and spacers summed up to 2.5 ± 1 mm. The cell was then crimped at $12.6 \cdot 10^{-1}$ T.

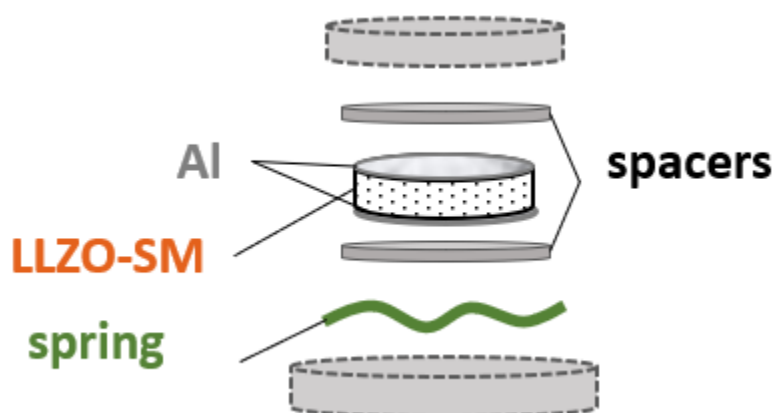


Figure 8. Coin cell assembly.

Electrochemical Impedance Spectroscopy Methodology

Electrochemistry Impedance spectroscopy (EIS) is a powerful non-destructive characterization technique that uses AC current, sweeping from very high to low frequency to measure the impedance (Z) of electrochemical cells. EIS accomplishes this by establishing a relationship to an equivalent circuit, shown in Figure 9a, and deriving the impedance from said circuit elements (i.e., resistance (R), double layer capacitance (C_{dl}), and a Warburg element (W)). This generates a Nyquist plot, shown in Figure 9b, which plots the imaginary impedance ($-ImZ$) vs the real impedance (ReZ). Using this information, the impedance for Li-ion diffusion can be calculated in the LLZO-SM composite by looking at the “tail”/ W element of the Nyquist plot, responsible for modeling Li-ion diffusion, and then extrapolating this slope to where it intersects on the real impedance axis. Using ReZ , the ionic conductivity (σ_{ion}) was calculated in the cell by obtaining the thickness (t) and the surface area (SA) of the LLZO-SM, shown in Equation 3 [37].

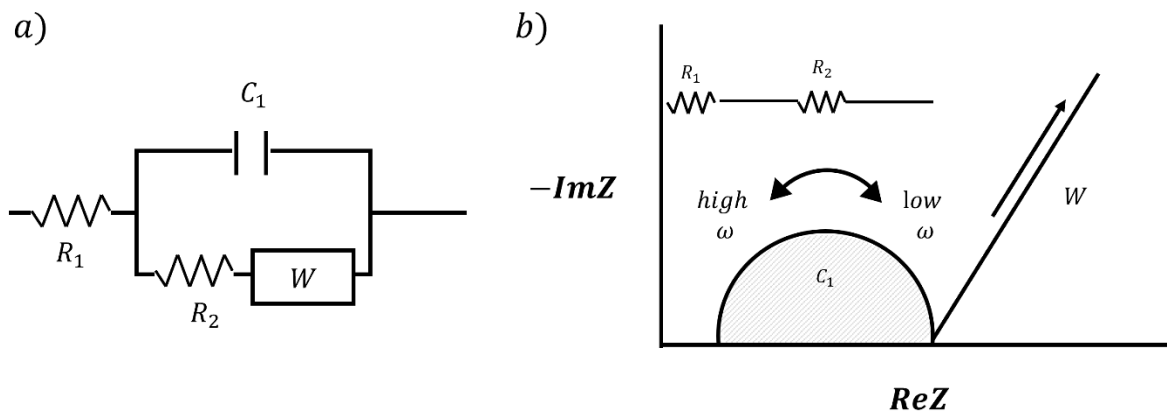


Figure 9. (a) Simplified EIS circuit model and (b) expected Nyquist plot.

$$\sigma_{ion} \left(\frac{S}{cm} \right) = \frac{t}{ReZ \cdot SA} \quad (3)$$

Reprocessed Half Cell Assembly Methodology

After conducting EIS and calculating the ionic conductivity of a sample, the coin cell was disassembled to recover as much LLZO-SM composite powder as possible in the same Ar backfilled glovebox using two pairs of pliers. The recovered powder was then weighed, and a weight lost (W_l) was calculated for the following procedural steps, where the recovered powder was divided by the original mass, shown in Equation 4.

$$W_l = \frac{m_{recovered}}{m_{pristine}} \quad (4)$$

The recovered powder then underwent a similar procedure outlined in “Pristine half Cell Assembly Methodology”, however instead of adding control solution and DMF, only $40 \mu L * W_l$ of DMF and $80 \mu L * W_l$ of acetonitrile were added – keeping the effective formulation of LLZO-SM consistent with respect to the LLZO-SM and PPC mass recovered.

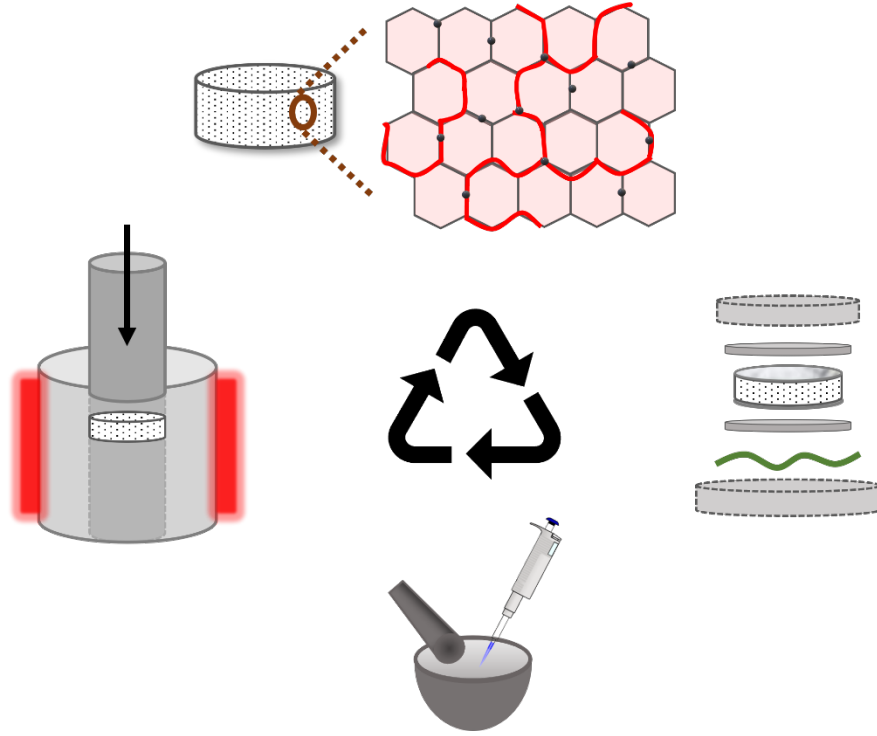


Figure 10. Recyclability loop of reprocessing LLZO-SM.

Li-ion Transport Activation Energy

To determine the activation energy (E_A) of Li-ion transport in LLZO-SM, the Nernst-Einstein relationship for conductivity was utilized, shown in Equation 5, wherein A is a pre-exponential factor, k_B is the Boltzmann constant, T is temperature in Kelvin, and σ_{ion} is Li-ion conductivity in $S \cdot cm^{-1}$. σ_{ion} was calculated using Equation 3. Two tests were conducted, one from $-50^\circ C$ through $100^\circ C$ held for 30s at $25^\circ C$ intervals, followed by the second from $-60^\circ C$ through $120^\circ C$ held for 5 mins at $20^\circ C$ intervals. The latter was performed as it was deemed 30s was not enough time for the furnace to thoroughly heat the contained system homogeneously.

$$\ln(\sigma T) = \ln A - \frac{E_a}{k_B T} \quad (5)$$

X-ray Diffraction of LLZO-SM Powder Methodology

LLZO-SM powder was prepared for X-ray diffraction (XRD) to determine the purity of the composition and illustrate the effect environment (i.e., humidity and air) has on LLZO-SM. First, the powder was finely grinded using a mortar and pestle. Then said powder was transferred into a silicon zero background holder (ZBH) mount, and leveled using a glass substrate. Any excess powder not level with the inslit on the ZBH was brushed away. The mount was then transferred to a Malvern Panalytical Empyrean III XRD, wherein using a divergence slit of $1/4^\circ$, a primary mask of 14mm, and a secondary mask of 14mm, the intensity vs 2θ data was collected at operating conditions 45kV and 40mA.

RESULTS AND DISCUSSION

The Viability of using Cold Sintering

The viability of using the cold sintering for reprocessing of LLZO-SM was determined using electrochemical impedance spectroscopy (EIS), shown in Figure 11. Figure 11a shows that the ReZ impedance of the pristine and reprocessed sample remained within the same order of magnitude, and therein illustrated, using Equation 3, the 1st reprocessed σ_{ion} 's only exhibited an <11% decrease. Further reprocessing revealed an overall decrease in the σ_{ion} as a function of reprocessed cycle, up to the third time, while maintaining consistent relative density – suggesting the cold sintering process is capable of densifying composite materials on a consistent basis. The relative density (RD) was calculated using Equation 6, where the ρ_o is the geometrically calculated density and ρ is 4.59 g/cm³, the theoretical density of the composite (ignoring DMF), calculated in Equation 7.

$$RD = \frac{\rho_o}{\rho} * 100\% \quad (6)$$

$$\rho = \rho_{c-LLZO} * vol\%_{c-LLZO} + \rho_{PPC} * vol\%_{PPC} + \rho_{LiClO_4} * vol\%_{LiClO_4} \quad (7)$$

However, from the 3rd to 4th and 5th reprocessing in Figure 11b, an unexpected increase in σ_{ion} was observed. This increase in σ_{ion} was speculated to be a result of a non-uniform sample thickness, thereby measuring lower impedances at decreased thickness across the composite, superficially increasing σ_{ion} . The procedural data for sample 1 is presented in Table 3.

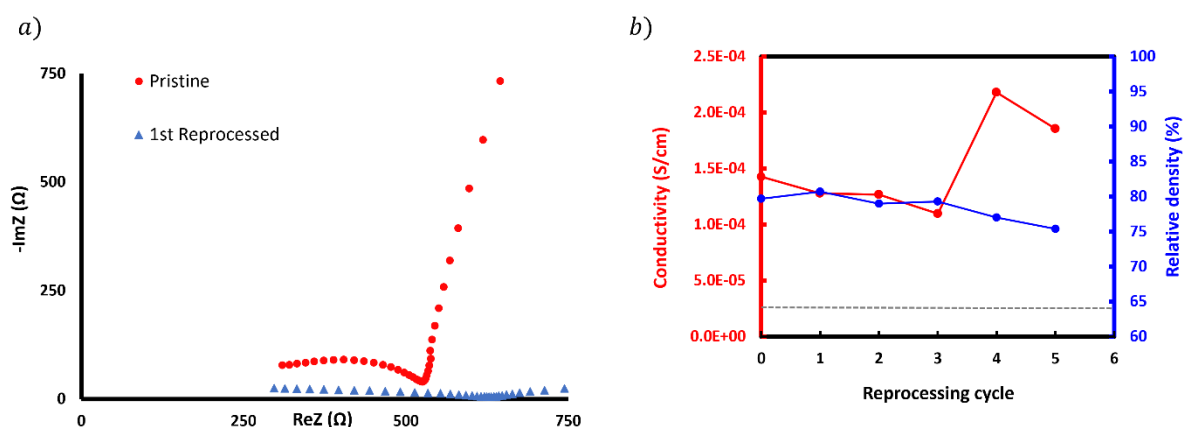


Figure 11. Sample 1 LLZO-SM composite (a) pristine vs reprocessed EIS curve and (b) reprocessed ionic conductivity (S/cm) and relative density (%) trend up to the fifth reprocessing.

Table 3. Sample 1 amount of acetonitrile (ACN), di-methylformamide (DMF), weight loss (W_1), thickness (t), mass (m), geometric density of the sample (ρ_o), relative density (RD), real impedance (ReZ), and ionic conductivity (σ_{ion}).

Reprocessing	0	1	2	3	4	5
ACN (μL)	120 (control soln)	69	57	51	47	44
DMF (μL)	40	35	29	25	23	22
W_1 (%)	N.A.	86.46	71.58	63.70	58.16	54.50
t (mm)	1.123	0.851	0.737	0.65	0.625	0.568
m (g)	0.5201	0.3992	0.3383	0.2995	0.2797	0.2488
ρ_o (g/cm^3)	3.49	3.54	3.46	3.47	3.37	3.30
RD %	76.06	77.04	75.38	75.67	73.49	71.93
ReZ (ohm)	621.8	525.6	459.1	467.9	226.6	241.7
σ_{ion} (S/cm)	1.43E-04	1.28E-04	1.27E-04	1.10E-04	2.18E-04	1.86E-04

Additional samples made following the same method of procedure also showed the same trend of increased conductivity during later cycles and consistent RD, shown in Figure 12 and Table 4,

giving stronger credence to the cold sintering process dependably sintering the composite, and indicating a homogeneously thinner SSE will offer a more optimized performance.

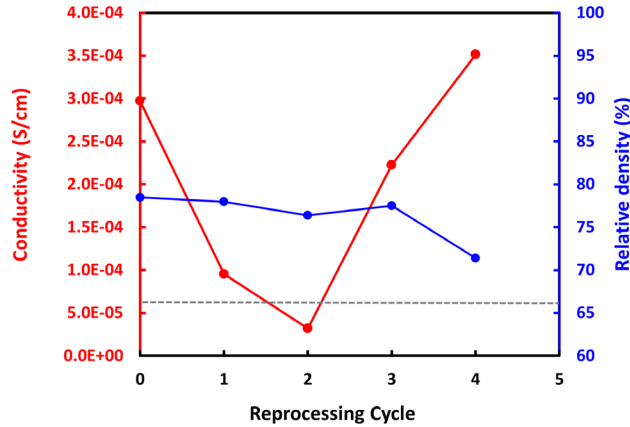


Figure 12. LLZO-SM composite sample 2 composite reprocessed ionic conductivity (S/cm) and relative density (%) trend up to the fourth reprocessing.

Table 4. Sample 2 amount of acetonitrile (ACN), di-methylformamide (DMF), weight loss (W_1), thickness (t), mass (m), geometric density of the sample (ρ_o), relative density (RD), real impedance (ReZ), and ionic conductivity (σ_{ion}).

Reprocessing	0	1	2	3	4
ACN (μL)	120 (control soln)	70	66	55	46
DMF (μL)	40	40	31	27	23
W_1 (%)	N.A.	86.46	71.58	63.70	58.16
t (mm)	1.074	0.902	0.823	0.661	0.669
m (g)	0.5131	0.4088	0.3654	0.2977	0.2776
ρ_o (g/cm^3)	3.60	3.58	3.51	3.56	3.28
RD %	78.46	77.99	76.40	77.50	71.40
ReZ (ohm)	285.3	746.2	2022	234.8	150.3
σ_{ion} (S/cm)	2.97E-04	9.55E-05	3.21E-05	2.22E-04	3.52E-4

Improving Ionic Conductivity

The initial decrease observed in early cycles of Figure 11b and Figure 12 was hypothesized to be caused by the formation of less conductive impurities, such as t-LLZO and Li_2CO_3 . Other known impurities of LLZO are shown in Table 5 [38].

Table 5. Common LLZO reactions when exposed to ambient conditions.

Reaction (assuming $x = 1/8$)	$\Delta G/\text{kJ mol}^{-1}$
$\text{Li}_{56}\text{La}_{24}\text{Zr}_{16}\text{O}_{96} + \text{H}_2\text{O}(\text{g}) \rightarrow \text{Li}_{55}\text{HLa}_{24}\text{Zr}_{16}\text{O}_{96} + \text{LiOH}$	-33.0
$\text{LiOH} + \frac{1}{2}\text{CO}_2(\text{g}) \rightarrow \frac{1}{2}\text{Li}_2\text{CO}_3 + \frac{1}{2}\text{H}_2\text{O}(\text{g})$	-33.6
$\text{Li}_{56}\text{La}_{24}\text{Zr}_{16}\text{O}_{96} + \text{H}_2\text{O}(\text{g}) \rightarrow \text{Li}_{54}\text{H}_2\text{La}_{24}\text{Zr}_{16}\text{O}_{96} + \text{Li}_2\text{O}$	+21.5
$\text{Li}_2\text{O} + \text{CO}_2(\text{g}) \rightarrow \text{Li}_2\text{CO}_3$	-147.6
$\text{Li}_{56}\text{La}_{24}\text{Zr}_{16}\text{O}_{96} + \text{H}_2\text{O}(\text{g}) \rightarrow \text{Li}_{54}\text{La}_{24}\text{Zr}_{16}\text{O}_{95} + 2\text{LiOH}$	+82.8
$\text{Li}_{56}\text{La}_{24}\text{Zr}_{16}\text{O}_{96} + \text{CO}_2(\text{g}) \rightarrow \text{Li}_{54}\text{La}_{24}\text{Zr}_{16}\text{O}_{95} + \text{Li}_2\text{CO}_3$	+15.6
$\text{Li}_{55}\text{HLa}_{24}\text{Zr}_{16}\text{O}_{96} + \frac{1}{2}\text{Li}_2\text{CO}_3 \rightarrow \text{Li}_{56}\text{La}_{24}\text{Zr}_{16}\text{O}_{96} + \frac{1}{2}\text{H}_2\text{O}(\text{g}) + \frac{1}{2}\text{CO}_2(\text{g})$	+66.6

To thermodynamically reverse the reaction of these phases, LLZO-SM powder was pre-heated prior to following the reprocessed methodology. The powder was transferred into half of a coin cell lid and placed on a hot plate for 1 hr at 150°C to induce an endothermic reaction to remove any LiOH or Li_2CO_3 . The results of reprocessing up to the fourth cycle are shown in Figure 13 and Table 6.

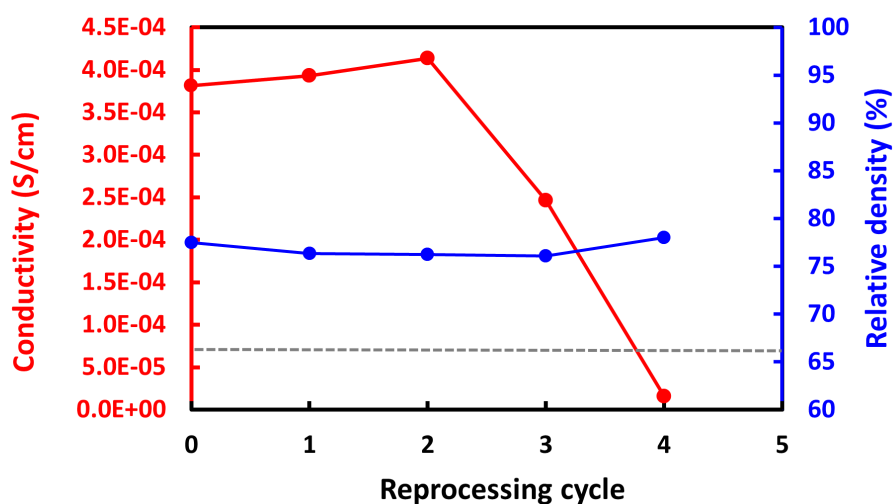


Figure 13. 150°C preheated LLZO-SM reprocessed ionic conductivity (S/cm) and relative density (%) trend up to the fourth reprocessing.

Table 6. Pre-heated LZO-SM samples amount of acetonitrile (ACN), di-methylformamide (DMF), weight loss (W_i), thickness (t), mass (m), geometric density of the sample (ρ_o), relative density (RD), real impedance (ReZ), and ionic conductivity (σ_{ion}).

Reprocessing	0	1	2	3	4
ACN (μL)	120 (control soln)	70	66	55	46
DMF (μL)	40	39	37	35	33
W (%)	N.A.	97.80	91.50	87.32	82.52
t (mm)	1.091	1.010	0.963	0.915	0.833
m (g)	0.5146	0.4696	0.447	0.4239	0.3956
ρ_o (g/cm ³)	3.56	3.50	3.50	3.49	3.58
RD %	77.46	76.36	76.23	76.08	77.99
ReZ (ohm)	226.1	203.1	183.9	293.7	4191
σ_{ion} (S/cm)	3.81E-04	3.93E-04	4.14E-04	2.46E-04	1.57E-05

From Figure 13, it is clear there is an initial benefit to pre-heating the LLZO-SM powder, as the ionic conductivity up to the second cycle increases above its starting point, but soon after rapidly declined – the reverse trend of LLZO-SM composites with no heat treatment. To compare all three samples, the relative conductivity (σ_{rel}) was calculated, by treating the pristine (i.e., 0 cycle) assembled conductivity as 100% and taking the ratio of a reprocessed cycles conductivity, shown in Equation 8.

$$\sigma_{rel} = \frac{\sigma_{cycle}}{\sigma_{pristine}} * 100\% \quad (8)$$

When the thicknesses and relative conductivities of each sample were compared, illustrated in Figure 14, the non-heated samples relative conductivities inflection points, at 0.650mm and 0.823mm respectively were thinner compared to the pre-heated samples final thickness of 0.833mm. From this observation, the reason the heated sample conductivity significantly decreased after initially increasing was inferred to be because the thickness of the sample was still too large for any significant contribution towards decreasing the overall impedance.

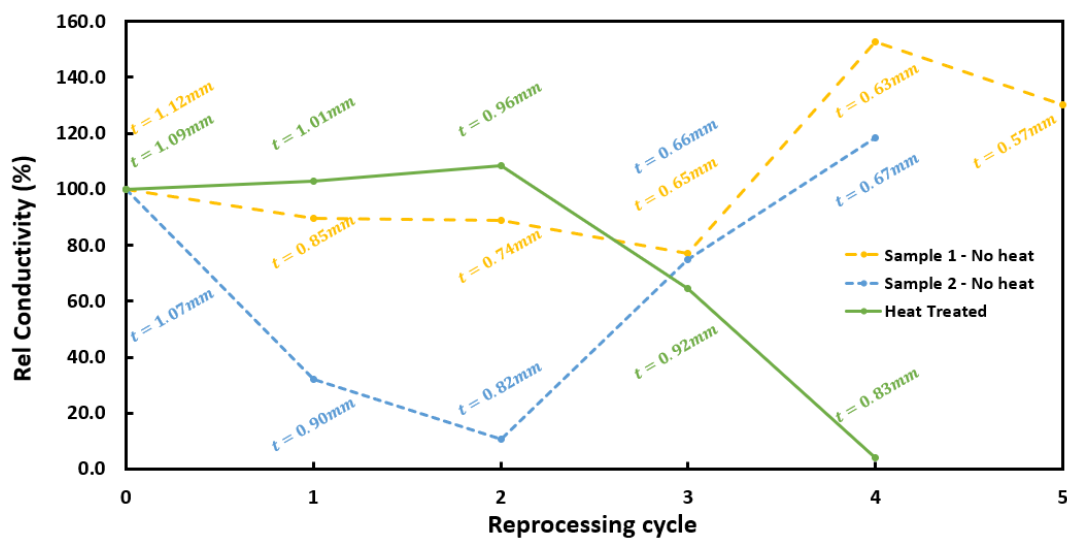


Figure 14. Comparing non-heated and heated LLZO-SM composite samples relative conductivity (%) and thicknesses (t) per reprocessing cycle.

Li-ion Transport Activation Energy

To ensure the LLZO-SM composite SSEs ionic conductivity was following the expected the Nernst-Einstein relationship regardless of whether the sample was heat treated or not, EIS was performed over two temperature ranges outlined in the Li-ion transport methodology. The results of a heated and non-heated LLZO-SM composite reprocessed conductivity as a function of temperature are shown in Figure 15a and 15b respectively.

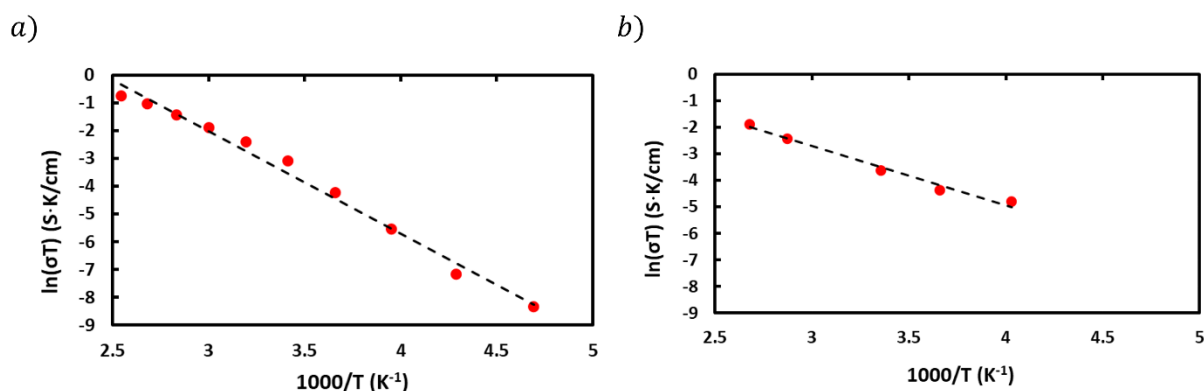


Figure 15. LLZO-SMs reprocessed conductivity as a function of temperature for a (a) heat treated and (b) non-heat-treated reprocessed sample.

Using Equation 5, the E_a of the heated sample was calculated to be $\cong 0.32$ eV, which falls slightly higher than the expected range stated by Wu et al., and the non-heat-treated samples was $\cong 0.19$ eV. Nevertheless, the fit of the line is still highly linear, proving with high confidence that both processes of reprocessing samples follow the expected Arrhenius behavior.

X-ray Diffraction Analysis

To emphasize the effect of LLZO-SMs environmental sensitivity and the thermodynamic reversibility of impurity phases, XRD was performed on pristine LLZO-SM powder, LLZO-SM powder exposed to 75% relative humidity (RH) for 92 hrs, LLZO-SM powder previously exposed to RH additionally exposed to ambient (STP) air for 118 hrs, and LLZO-SM powder exposed to RH and STP heated as described above at 200°C for 19 hrs, shown in Figure 16 below.

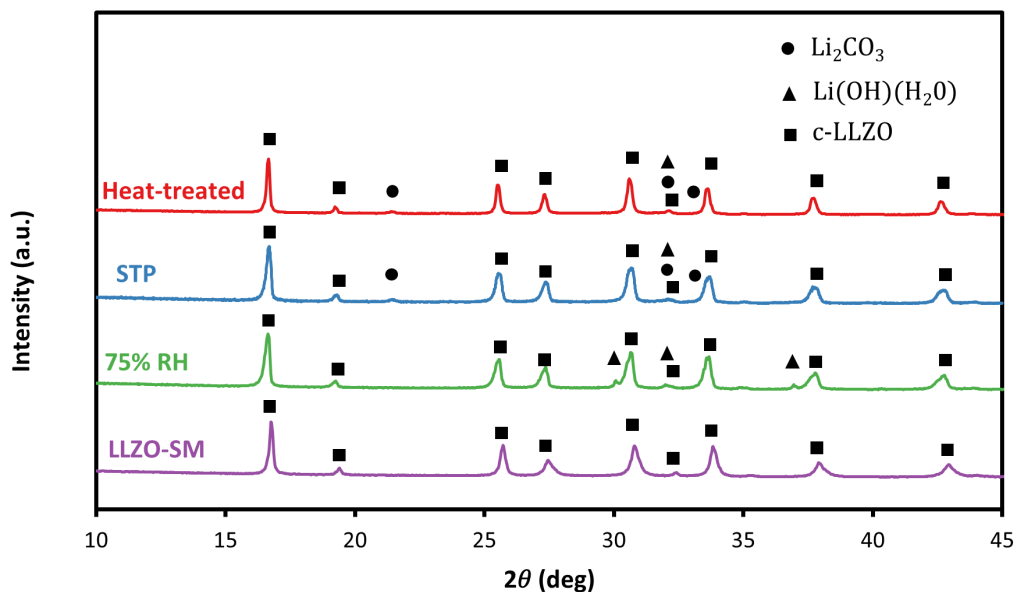


Figure 16. XRD analysis of LLZO-SM powder exposed to relative humidity (RH), RH and ambient conditions (STP), and RH, STP, and heat-treatment.

As illustrated in Table 5, LLZO-SM powder is sensitive to moisture, and studies have shown the formation of LiOH and Li_2CO_3 have detrimental impacts on the ionic conductivity of c-LLZO [38]. In this experiment, we emphasize the spontaneous nature of both LiOH and Li_2CO_3 reactions in a humid environment and ambient conditions respectively, stressing the importance of ensuring these contaminants are not present in c-LLZO. First, the provided LLZO-SM powder was confirmed to be c-LLZO, shown in Figure 16. Then, after 92 hrs of exposure to 75% RH, the presence of LiOH(H_2O) was confirmed, most notably at $30^\circ 2\theta$. Afterwards, the LLZO-SM powder containing LiOH(H_2O) was exposed to ambient temperature and pressure for 118 hrs, resulting in the formation of Li_2CO_3 , illustrated predominantly at $21.5^\circ 2\theta$, with the presence of LiOH(H_2O) significantly decreased, as can be seen with the disappearance of the $30^\circ 2\theta$ peak. The decrease in LiOH(H_2O) was expected, as it is a reactant used in forming Li_2CO_3 . Finally, the contaminated powder was then heat-treated following the same procedure used above.

Unfortunately, the presence of both $\text{LiOH}(\text{H}_2\text{O})$ and Li_2CO_3 still remained. Furthermore, we conclude that while heat treating the LLZO-SM powder at 150°C when never directly exposed to RH or ambient conditions did increase ionic conductivity during initial reprocess cycling, the hot plate heating methodology is insufficient in diminishing the bulk presence of contaminants when deliberately introduced. Moreover, to achieve the desired results of no $\text{LiOH}(\text{H}_2\text{O})$ and Li_2CO_3 contaminants, we suggest using an oven in a non-oxidizing environment with a more uniform heating profile.

CONCLUSIONS

In this study, the viability of using cold sintering to recycle/reprocess the composite material system LLZO-SM-PPC-LiClO₄ for SSE battery applications was reported. Given the provided data, we conclude that cold sintering is an effective process for maintaining consistent relative density, however further improvements in maintaining consistent ionic conductivity still need to be explored.

One such method suggested in this study was heat treating the LLZO-SM powder prior to cold sintering to remove unwanted, less conductive phases. The conductivity data shown on this approach when the powders history was only in an Ar environment, heated to 150°C, demonstrated an increased ionic conductivity in the early reprocessing cycles, ranging between $3 - 4 \times 10^{-4} S/cm$, compared to the non-heated powders performance ranging from $1 - 2 \times 10^{-4} S/cm$. However, the heat-treated powders ionic conductivity dramatically decreased shortly thereafter the early reprocessing cycles. Further analysis of the samples revealed that the thickness of the pellet is hypothesized to play a key role in achieving a desirably low impedance, and therefore additional studies need to be explored pertaining to cold sintering and optimal pellet thickness to achieve consistently high ionic conductivity. Additionally, XRD analysis confirmed that the same heat treatment process did not effectively remove deliberately introduced impurities, such as LiOH and Li₂CO₃, from contaminated LLZO-SM powder even after 19 hrs of treatment, due to insufficient heat transfer to the bulk powder. It is therefore recommended that future studies involving heat-treating contaminated LLZO-SM powder should not be conducted on a hot plate, which lacks sufficient thermal insulation to ensure the LLZO-SM powder is uniformly being heated.

BIBLIOGRAPHY

- [1] Tarascon, J.-M., & Armand, M. (2001). Issues and challenges facing rechargeable lithium batteries. *Nature*, *414*(6861), 359–367. <https://doi.org/10.1038/35104644>.
- [2] Scrosati, B., & Garche, J. (2010). Lithium batteries: Status, prospects and future. *Journal of Power Sources*, *195*(9), 2419–2430. <https://doi.org/10.1016/j.jpowsour.2009.11.048>.
- [3] Balakrishnan, P. G., Ramesh, R., & Prem Kumar, T. (2006). Safety mechanisms in lithium-ion batteries. *Journal of Power Sources*, *155*(2), 401–414. <https://doi.org/10.1016/j.jpowsour.2005.12.002>.
- [4] *Lithium-Ion Battery Market Size, Share & Trends Analysis Report by Product (LCO, LFP, NCA, LMO, LTO, Lithium Nickel Manganese Cobalt), by Application, by Region, and Segment Forecasts, 2020–2027*; Research and Markets: 2020.
- [5] Han, F., Zhu, Y., He, X., Mo, Y., & Wang, C. (2016). Electrochemical stability of $\text{Li}_{10}\text{GeP}_2\text{S}_{12}$ and $\text{Li}_7\text{La}_3\text{Zr}_2\text{O}_{12}$ solid electrolytes. *Advanced Energy Materials*, *6*(8), 1501590. <https://doi.org/10.1002/aenm.201501590>
- [6] Li, J., Ma, C., Chi, M., Liang, C., & Dudney, N. J. (2014). Solid electrolyte: The key for high-voltage lithium batteries. *Advanced Energy Materials*, *5*(4), 1401408. <https://doi.org/10.1002/aenm.201401408>
- [7] Balaish, M., Gonzalez-Rosillo, J. C., Kim, K. J., Zhu, Y., Hood, Z. D., & Rupp, J. L. (2021). Processing thin but robust electrolytes for solid-state batteries. *Nature Energy*, *6*(3), 227–239. <https://doi.org/10.1038/s41560-020-00759-5>
- [8] Tikekar, M. D., Choudhury, S., Tu, Z., & Archer, L. A. (2016). Design principles for electrolytes and interfaces for stable lithium-metal batteries. *Nature Energy*, *1*(9). <https://doi.org/10.1038/nenergy.2016.114>
- [9] Murugan, R., Thangadurai, V., & Weppner, W. (2007). Fast lithium ion conduction in garnet-type $\text{Li}_7\text{La}_3\text{Zr}_2\text{O}_{12}$. *Angewandte Chemie International Edition*, *46*(41), 7778–7781. <https://doi.org/10.1002/anie.200701144>
- [10] Wu, J.-F., Chen, E.-Y., Yu, Y., Liu, L., Wu, Y., Pang, W. K., Peterson, V. K., & Guo, X. (2016). Gallium-doped $\text{Li}_7\text{La}_3\text{Zr}_2\text{O}_{12}$ garnet-type electrolytes with high lithium-ion conductivity. *ACS Applied Materials & Interfaces*, *9*(2), 1542–1552. <https://doi.org/10.1021/acsami.6b13902>
- [11] Chen, F., Li, J., Huang, Z., Yang, Y., Shen, Q., & Zhang, L. (2018). Origin of the phase transition in lithium garnets. *The Journal of Physical Chemistry C*, *122*(4), 1963–1972. <https://doi.org/10.1021/acs.jpcc.7b10911>

- [12] Jonderian, A., & McCalla, E. (2021). The role of metal substitutions in the development of Li Batteries, part II: Solid electrolytes. *Materials Advances*, 2(9), 2846–2875. <https://doi.org/10.1039/d1ma00082a>
- [13] Lee, W., Lyon, C. K., Seo, J. H., Lopez-Hallman, R., Leng, Y., Wang, C. Y., Hickner, M. A., Randall, C. A., & Gomez, E. D. (2019). Ceramic–salt composite electrolytes from Cold Sintering. *Advanced Functional Materials*, 29(20), 1807872. <https://doi.org/10.1002/adfm.201807872>
- [14] Seo, J.-H., Nakaya, H., Takeuchi, Y., Fan, Z., Hikosaka, H., Rajagopalan, R., Gomez, E. D., Iwasaki, M., & Randall, C. A. (2020). Broad temperature dependence, high conductivity, and structure-property relations of Cold Sintering of LLZO-based composite electrolytes. *Journal of the European Ceramic Society*, 40(15), 6241–6248. <https://doi.org/10.1016/j.jeurceramsoc.2020.06.050>
- [15] Cao, S., Song, S., Xiang, X., Hu, Q., Zhang, C., Xia, Z., Xu, Y., Zha, W., Li, J., Gonzale, P. M., Han, Y.-H., & Chen, F. (2019). Modeling, preparation, and elemental doping of $\text{Li}_7\text{La}_3\text{Zr}_2\text{O}_{12}$ garnet-type solid electrolytes: A Review. *Journal of the Korean Ceramic Society*, 56(2), 111–129. <https://doi.org/10.4191/kcers.2019.56.2.01>
- [16] Dumon, A., Huang, M., Shen, Y., & Nan, C.-W. (2013). High Li ion conductivity in strontium doped $\text{Li}_7\text{La}_3\text{Zr}_2\text{O}_{12}$ garnet. *Solid State Ionics*, 243, 36–41. <https://doi.org/10.1016/j.ssi.2013.04.016>
- [17] M., B. S., & Roy, J. (2011). The effect of strontium doping on densification and electrical properties of $\text{Ce}_{0.8}\text{Gd}_{0.2}\text{O}_{2-\delta}$ electrolyte for it-SOFC application. *Ionics*, 18(3), 291–297. <https://doi.org/10.1007/s11581-011-0633-4>
- [18] Guo, J., Floyd, R., Lowum, S., Maria, J.-P., Herisson de Beauvoir, T., Seo, J.-H., & Randall, C. A. (2019). Cold sintering: Progress, challenges, and future opportunities. *Annual Review of Materials Research*, 49(1), 275–295. <https://doi.org/10.1146/annurev-matsci-070218-010041>
- [19] Berg, H. (2015). The electrochemical cell. In *Batteries for Electric Vehicles: Materials and Electrochemistry* (pp. 7-46). Cambridge: Cambridge University Press. doi:10.1017/CBO9781316090978.004
- [20] Wang, Q., Jiang, L., Yu, Y., & Sun, J. (2019). Progress of enhancing the safety of lithium ion battery from the electrolyte aspect. *Nano Energy*, 55, 93-114. doi:10.1016/j.nanoen.2018.10.035
- [21] Davoodabadi, A., Jin, C., Wood III, D. L., Singler, T. J., & Li, J. (2020). On electrolyte wetting through lithium-ion battery separators. *Extreme Mechanics Letters*, 40, 100960. doi:10.1016/j.eml.2020.100960

- [22] Landt Instruments. (2021, April 17). *How to make Coin Cells*. Landt Instruments. Retrieved 2021, from <https://www.landtinst.com/how-to-make-coin-cells/>
- [23] AOT. (2006). *Aluminum laminated film for lab pouch cell case preparation*. Lithium Ion Battery Raw Material Aluminum Laminated Film for Pouch Cell Case. Retrieved 2021, from <https://www.aotbattery.com/product/Aluminum-Laminated-Film-for-Lab-Pouch-Cell-Case-Making.html>
- [24] Lam, M. (2019, November 29). *Advantages of pouch cell battery, trend and opportunities*. Medium. Retrieved 2021, from <https://medium.com/battery-lab/advantages-of-pouch-cell-battery-trend-and-opportunities-d08a5f0c6804>
- [25] Elecorev Energy. (2021, October 14). *Prismatic lithium cells*. Elecorev Energy. Retrieved 2021, from <https://elecorevenergy.com/prismatic-lithium-cells/>
- [26] Awaka, J., Takashima, A., Kataoka, K., Kijima, N., Idemoto, Y., & Akimoto, J. (2011). Cheminform abstract: Crystal structure of fast lithium-ion-conducting cubic $\text{Li}_7\text{La}_3\text{Zr}_2\text{O}_{12}$. *ChemInform*, 42(18). <https://doi.org/10.1002/chin.201118004>
- [27] Awaka, J., Kijima, N., Hayakawa, H., & Akimoto, J. (2009). Synthesis and structure analysis of tetragonal $\text{Li}_7\text{La}_3\text{Zr}_2\text{O}_{12}$ with the garnet-related type structure. *Journal of Solid State Chemistry*, 182(8), 2046–2052. <https://doi.org/10.1016/j.jssc.2009.05.020>
- [28] Raju, M. M., Altayran, F., Johnson, M., Wang, D., & Zhang, Q. (2021). Crystal structure and preparation of $\text{Li}_7\text{La}_3\text{Zr}_2\text{O}_{12}$ (LLZO) solid-state electrolyte and doping impacts on the conductivity: An overview. *Electrochem*, 2(3), 390–414. <https://doi.org/10.3390/electrochem2030026>
- [29] Song, S., Sheptyakov, D., Korsunsky, A. M., Duong, H. M., & Lu, L. (2016). High Li ion conductivity in a garnet-type solid electrolyte via unusual site occupation of the doping cations. *Materials & Design*, 93, 232–237. <https://doi.org/10.1016/j.matdes.2015.12.149>
- [30] Gonzalez Puente, P. M., Song, S., Cao, S., Rannalter, L. Z., Pan, Z., Xiang, X., Shen, Q., & Chen, F. (2021). Garnet-type solid electrolyte: Advances of ionic transport performance and its application in all-solid-state batteries. *Journal of Advanced Ceramics*, 10(5), 933–972. <https://doi.org/10.1007/s40145-021-0489-7>
- [31] Song, S., Kotobuki, M., Zheng, F., Xu, C., Wang, Y., Li, W. D., Hu, N., & Lu, L. (2016). Roles of alkaline earth ions in garnet-type superionic conductors. *ChemElectroChem*, 4(2), 266–271. <https://doi.org/10.1002/celec.201600639>
- [32] Mori, D., Sugimoto, K., Matsuda, Y., Ohmori, K., Katsumata, T., Taminato, S., Takeda, Y., Yamamoto, O., & Imanishi, N. (2018). Synthesis, structure and ionic conductivity of garnet like lithium ion conductor $\text{Li}_{6.25+x}\text{Ga}_{0.25}\text{La}_{3-x}\text{Sr}_x\text{Zr}_2\text{O}_{12}$. *Journal of The Electrochemical Society*, 166(3). <https://doi.org/10.1149/2.0171903jes>

- [33] Xue, W., Yang, Y., Yang, Q., Liu, Y., Wang, L., Chen, C., & Cheng, R. (2018). The effect of sintering process on lithium ionic conductivity of $\text{Li}_{6.4}\text{Al}_{0.2}\text{La}_3\text{Zr}_2\text{O}_{12}$ garnet produced by solid-state synthesis. *RSC Advances*, 8(24), 13083–13088. <https://doi.org/10.1039/c8ra01329b>
- [34] Guo, H., Baker, A., Guo, J., & Randall, C. A. (2016). Cold sintering process: A novel technique for low-temperature ceramic processing of ferroelectrics. *Journal of the American Ceramic Society*, 99(11), 3489–3507. <https://doi.org/10.1111/jace.14554>
- [35] Yu, T., Cheng, J., Li, L., Sun, B., Bao, X., & Zhang, H. (2019). Current understanding and applications of the Cold Sintering Process. *Frontiers of Chemical Science and Engineering*, 13(4), 654–664. <https://doi.org/10.1007/s11705-019-1832-1>
- [36] Ndayishimiye, A., Sengul, M. Y., Sada, T., Dursun, S., Bang, S. H., Grady, Z. A., Tsuji, K., Funahashi, S., van Duin, A. C. T., & Randall, C. A. (2020). Roadmap for densification in cold sintering: Chemical pathways. *Open Ceramics*, 2, 100019. <https://doi.org/10.1016/j.oceram.2020.100019>
- [37] Middlemiss, L. A., Rennie, A. J. R., Sayers, R., & West, A. R. (2020). Characterisation of batteries by electrochemical impedance spectroscopy. *Energy Reports*, 6, 232–241. <https://doi.org/10.1016/j.egy.2020.03.029>
- [38] Sharafi, A., Yu, S., Naguib, M., Lee, M., Ma, C., Meyer, H. M., Nanda, J., Chi, M., Siegel, D. J., & Sakamoto, J. (2017). Impact of air exposure and surface chemistry on $\text{Li-Li}_7\text{La}_3\text{Zr}_2\text{O}_{12}$ Interfacial Resistance. *Journal of Materials Chemistry A*, 5(26), 13475–13487. <https://doi.org/10.1039/c7ta03162a>

ACADEMIC VITA
Anthony P. Romero

anthony.romero@outlook.com

EDUCATION

The Pennsylvania State University, University Park PA
Schreyer Honors College
Bachelor of Science in Materials Science & Engineering
Minor in Nanotechnology

Aug. 2018 – May 2022
June 2020 – May 2022

RESEARCH INTEREST

Battery Science: I am interested in expanding the boundaries of knowledge regarding characterization and processing of battery materials to commercialize electric vehicles & grid energy storage.

ACADEMIC RESEARCH EXPERIENCE

Honors Thesis: The Recyclability Potential of LLZO Solid-State Composite Electrolytes, State College, PA – Dr. Enrique Gomez

Aug. 2021– Present

- Measuring ionic conductivity utilizing electrochemical impedance spectroscopy (EIS)
- Studying phase evolution of recycled LLZO using x-ray diffraction (XRD)
- Efficiently synthesizing, assembling, & dismantling composite coin cells in a glove box environment
- Experimentally investigating heat treatment during reprocessing towards improving ionic conductivity

The Relationship Between Enthalpy Landscapes & Elastic Modulus of Soda-Lime Glass, McMurray, PA – Dr. Collin Wilkinson

May 2020 – Aug. 2020

- Assessed relevant literature to propose methods of procedure & test hypothesis with generated data
- Encoded script to predict cracking behavior utilizing Large-scale Atomic/Molecular Massively Parallel Simulator (LAMMPS)
- Modeled soda-lime glass material behavior under pressure using visualization & analysis software OVITO

MXene Electrode Materials for Electrochemical Energy Storage: First-Principles & Grand Canonical Monte Carlo Simulations, State College, PA – Dr. Ismaila Dabo

Sept. 2019 – May 2020

- Investigated MXenes electrochemical potential varying surface terminations utilizing density functional theory (DFT), cluster expansions, & grand canonical Monte Carlo
- Modeled MXenes electrostatic potentials & electron charge densities in VESTA
- Analyzed MXenes ideal ground state structures implementing DFT

INDUSTRY EXPERIENCE

Battery Research & Development Intern, The Battery Innovation Center, Newberry, IN – Dr. James Fleetwood

May 2021 – Aug. 2021

- Lead a team of 9 on a Hopper battery slurry upgrade project, increasing slurry capacity from 2L to 6L employing a positive team-oriented attitude & reacting swiftly to setbacks
- Evaluated Li-ion battery's material properties & performance through applying electrochemical processes & chemistry knowledge
- Fabricated over 100 battery slurry mixes, electrode film coatings, half coin cells, full coin cells, & pouch cells
- Articulated a straightforward & concise SOP for an ECC-Opto-Std to visualize lithiation in anodes

LEADERSHIP/ EXTRACURRICULARS

Vice President of Minorities in Earth & Mineral Science – Student Organization May 2021 – Present

- Planning social & educational events striving to foster community & professional development
- Creating eye-grabbing flyers in Adobe Spark for events

Senior Representative for Materials Advantage (MA)– Student Chapter Professional Society in Materials Science May 2021 – Present

- MA provides professional development, industry & research exposure, & community building
- Assisting in planning all professional, social, & volunteer activities

Earth & Mineral Science College Ambassador Aug. 2020 – Present

- Aiding prospective & current students with involvement, research, & general life in the college

Earth & Mineral Science Peer Mentor Aug. 2019 – Aug. 2020

- Provided personal guidance & academic resources to aid a rising freshman in EMS

COMPUTATIONAL SKILLS

- | | | |
|--------------------|----------|----------|
| • Microsoft Office | • Linux | • Python |
| • OVITO | • LAMMPS | • R |
| | • MATLAB | • VESTA |
-

PRESENTATIONS

The Recyclability Potential of LLZO Solid-State Composite Electrolytes March 2022
Penn State Materials Science and Engineering Undergraduate Poster Competition

How to Make Solar Energy Economical Nov. 2018
Penn State Earth & Mineral Science Undergraduate Poster Exhibition

HONORS

Penn State Metallurgy Alumni Scholarship Aug. 2021
The Pennsylvania State University Dept. of Materials Science & Engineering

Jack D. Ramaley Undergraduate Scholarship Fund in MatSE Aug. 2020
The Pennsylvania State University Dept. of Materials Science & Engineering

William & Estelle Turney Scholarship in Ceramic Science & Engineering Aug. 2020
The Pennsylvania State University Dept. of Materials Science & Engineering

Rosemarie C. & Howard R. Peiffer Scholarship Aug. 2019
The Pennsylvania State University Dept. of Materials Science & Engineering

Matthew J. Wilson Honors Scholarship July 2019
The Pennsylvania State University College of Earth & Mineral Sciences

Anthony J. & Alberta L. Perrotta Scholarship Feb. 2019
The Pennsylvania State University Dept. of Materials Science & Engineering

Dean's List Aug. 2018 – Present
The Pennsylvania State University College of Earth & Mineral Sciences

Matthew J. Wilson Honors Scholarship Aug. 2018
The Pennsylvania State University College of Earth & Mineral Sciences

AWARDS

1st Place – Undergraduate Materials Science and Engineering Poster Competition March 2022

The Pennsylvania State University Dept. of Materials Science & Engineering

College of Earth and Mineral Sciences Academy for Global Excellence (EMSAGE) Feb. 2022

The Pennsylvania State University Student Engagement

- Recognizes students who have attained significant achievements in scholarship, experiential learning and global literacy, and service.

The Graduate Education for Minorities (GEM) PhD Fellowship Dec. 2021

The National GEM Consortium

- Fellowship awarded to high quality underrepresented students looking to pursue masters and doctoral degrees in applied science and engineering.

Summer Research Opportunity Program (SROP) Professional Development Cohort June 2020

Big 10 Academic Alliance, The Pennsylvania State University

- Eight-week professional development opportunity designed to prepare talented undergraduate students from underrepresented groups for graduate study

Student Engagement Network Remote Innovation Grant May 2020

The Pennsylvania State University Student Engagement

- Grant awarded to Penn State students funding summer research experiences that make a personal &/or community impact.

Bunton-Waller Undergraduate Fellowship Aug. 2018

The Pennsylvania State University Office of the Vice Provost for Ed. Equity

- Fellowship awarded to student who demonstrated academic potential & enhance the broad & diverse student population at Penn State

PROFESSIONAL MEMBERSHIPS

- Materials Advantage – Penn State Chapter
- American Ceramic Society (ACerS)
- The Minerals, Metals & Materials Society (TMS)
- Association for Iron & Steel Technology (AIST)
- Advanced Materials & Processes (ASM)
- PHI ETA SIGMA National Honor Society